Creation of Liquid Metal 3D Microstructures Using Dielectrophoresis

Shi-Yang Tang, Jiuyang Zhu, Vijay Sivan, Berrak Gol, Rebecca Soffe, Wei Zhang, Arnan Mitchell,* and Khashayar Khoshmanesh**

Patterning customized arrays of microscale Galinstan or EGaIn liquid metals enables the creation of a variety of microfabricated systems. Current techniques for creating microsized 3D structures of liquid metals are limited by the large dimension or low aspect ratio of such structures, and time-consuming processes. Here, a novel technique for creating 3D microstructures of Galinstan using dielectrophoresis is introduced. The presented technique enables the rapid creation of Galinstan microstructures with various dimensions and aspect ratios. Two series of proof-of-concept experiments are conducted to demonstrate the capabilities of this technique. First, the 3D Galinstan microstructures are utilized as 3D microelectrodes to enhance the trapping of tungsten trioxide (WO_3) nanoparticles flowing through a microfluidic channel. Second, the patterned Galinstan microstructures are utilized as microfins to improve the dissipation of heat within a microfluidic channel that is located onto a hot spot. The presented technique can be readily used for creating customized arrays of 3D Galinstan microstructures for a wide range of applications.

1. Introduction

Gallium based eutectic liquid metals (LMs) including EGaIn (75% gallium and 25% indium)[1] and Galinstan (68.5% gallium, 21.5% indium, and 10% tin)[2] possess remarkable properties such as high electrical conductivity, high thermal conductivity, high surface tension, extremely low vapor pressure, and low toxicity in comparison to mercury.[2] These properties make them attractive for the development of stretchable or reconfigurable components,[3–5] soft electronics,[6,7] chemical sensors,[8,9] photocatalysts,[8,10] as well as small-scale devices such as pumps[11] and mixers.[12,13]

These liquid metals form a thin (≈1 nm) skin of oxide layer which is mainly composed of gallium oxide upon exposure to air.[2] This oxide layer not only allows liquid metal to stick to the surface of materials such as glass, metal, silicon, and paper, but also mechanically stabilizes the liquid metal in stable, nonequilibrium shapes, and thus facilitating it to be patterned using many techniques, including filling into microfluidic channel,[13] printing using various techniques,[14–16] molding,[17] and directly writing onto surfaces.[18,19] Using the direct filling method, liquid metal can be directly injected into a patterned microfluidic channel to form electrodes.[13] This avoids complicated processes such as deposition, photolithography, and etching required for patterning conventional solid electrodes. However, the dimension of liquid metal electrodes is relatively large.[10] Methods such as stencil, contact, and spray printing allow patterning large scare, thin layer of liquid metal onto various substrates. However, creating 3D microstructures with aspect ratios larger than 0.5 using printing methods is limited by the thickness of stencil, resolution of printer, and the surface tension limitation of the liquid metal itself.[14,15] Molding technique allows for patterning an array of liquid metal spheres with various sizes.[17] However, the size of the liquid metal spheres produced using this technique is limited to ≈100 µm.[17] Using direct writing method, 3D structures of EGaIn have been fabricated by stacking liquid metal onto a substrate through a computer-controlled syringe,[19] in which the 3D structures are stabilized by the native oxide layer formed on the surface of liquid metal. However, the features obtained using this method are around 200 µm,[19] which are still too large to be implemented into microfluidic devices. Additionally, fabricating a large amount of 3D structures simultaneously using this method could be time consuming.[19] In the absence of such thin oxide layer, liquid metals can also be patterned by manual injecting using a pipette.[12] However, submillimeter patterning can hardly be achieved and the control over the uniformity is difficult using this method.[12]

Microfluidic devices with 3D microstructures are widely used to enhance the efficiency, reliability, and overall performance of such systems. For example, 3D structures including grooves or barriers have been used to induce secondary flows along the main flow, and eventually enhance the mixing efficiency of microfluidic devices.[20,21] 3D microelectrodes have been utilized to improve the flow rate and frequency range of AC electro-osmotic pumps,[22] and also to enhance the trapping or sorting efficiency of cells using dielectrophoresis (DEP).[23,24]

S.-Y. Tang, J. Zhu, Dr. V. Sivan, B. Gol, R. Soffe, W. Zhang, Prof. A. Mitchell, Dr. K. Khoshmanesh
School of Electrical and Computer Engineering
RMIT University
VIC 3001, Australia
E-mail: shiyang.tang@rmit.edu.au;
arnan.mitchell@rmit.edu.au;
khashayar.khoshmanesh@rmit.edu.au

DOI: 10.1002/adfm.201501296

However, these advantages come with a price as the conventional methods such as etching and lithography for fabricating 3D microstructures is rather complicated and time consuming, in which multiple processes and dedicated equipment are needed, and hazardous materials such as hydrofluoric acid are also required during the process.[25]

In this work, we develop a novel method for creating 3D microstructures by immobilizing Galinstan microdroplets onto planar chromium/gold microelectrode pads using dielectrophoresis. The capability of this method for creating 3D microstructures with various aspect ratios and sizes is demonstrated. We further utilize the created 3D microstructures to form an array of 3D microelectrodes in order to trap tungsten trioxide (WO_3) nanoparticles within a microfluidic channel. Moreover, we utilize such Galinstan 3D microstructures to improve the convective heat transfer within a microfluidic channel.

2. Creating Liquid Metal 3D Microstructures

Our presented technique for creating Galinstan 3D microstructures onto a planar DEP platform consists of three major steps, as explained here.

Step one: The Galinstan microdroplet suspension is obtained by ultrasonication method.[8,26] To achieve this, a 10 µL droplet of Galinstan is added into a glass bottle containing 2 mL deionized (DI) water (**Figure 1**A), and is sonicated in an ultrasonication bath for 5 min. The sonication disintegrates the large Galinstan droplet into microdroplets (Figure 1B), while the native oxide layer formed on the surface of each Galinstan microdroplet prevents merging of the formed microdroplets after sonication.[8,26] This oxide layer is thin, ranging from 0.7 to 3 nm when exposed to ambient oxygen, as obtained by X-ray reflectometry (XRR) or X-ray photoelectron spectroscopy (XPS) techniques.[27–29] The size distribution of Galinstan microdroplets is determined using scanning electron microscopy (SEM), as detailed in Figure S1 (Supporting Information). Our measurements indicate that the diameter of microdroplets is mainly distributed between 0.1 and 3.5 µm, with the average size of microdroplets being around 2 µm. Our extended SEM imaging indicates that the obtained Galinstan microdroplets remain stable in DI water for up to 6 h after the ultrasonication process, with no merging occurs between them, and the size distribution of microdroplets remained almost unchanged (see Figure S1 in the Supporting Information). Next, 4 mg of sodium dodecyl sulfate (SDS) is added into the suspension to prevent Galinstan microdroplets sticking to the glass.

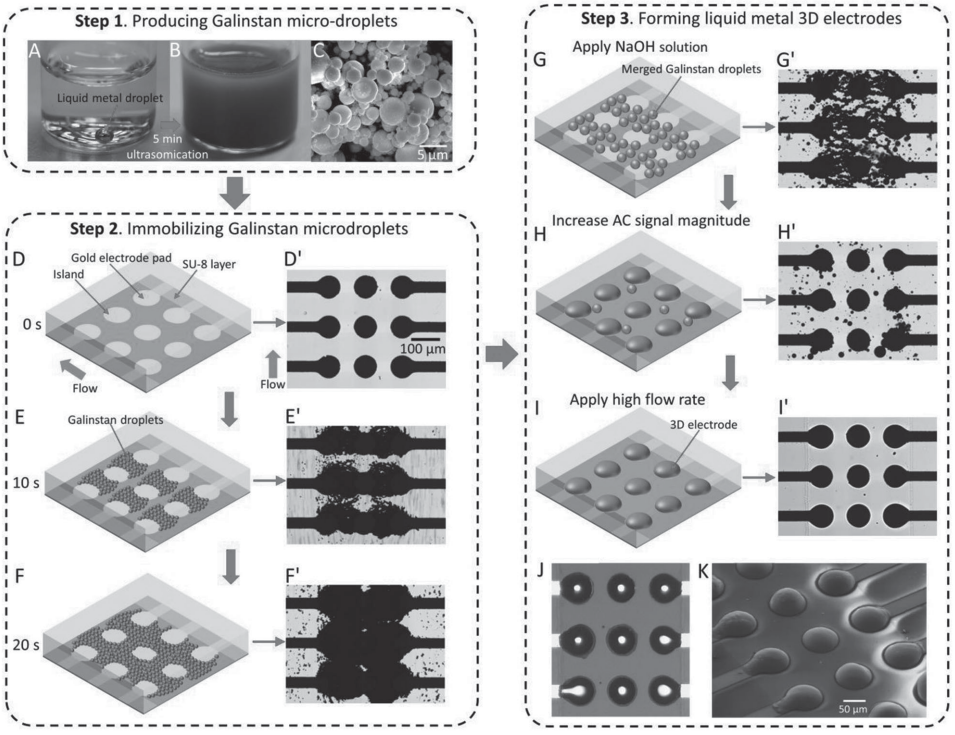

Figure 1. Procedure for obtaining Galinstan 3D microstructures. A) A 10 µL Galinstan droplet is added into a glass bottle which contains 2 mL DI water. B) Obtained Galinstan microdroplet suspension after 5 min ultrasonication. C) SEM images for the obtained micro- to nanosized Galinstan droplets. D,D′) Schematic and actual image of the patterned DEP microelectrodes. Schematic and actual image for the immobilized Galinstan microdroplets E,E′) 10 s and F,F′) 20 s after activating the electric field when the Galinstan droplet suspension is added. G,G′) Schematic and actual image for the merging of immobilized Galinstan microdroplets after applying NaOH solution with a concentration of 0.1 mol L^{-1}. H,H′) Schematic and actual image for the formation of Galinstan 3D microstructures after increasing the magnitude of the applied signal to 10 V. I,I′) Schematic and actual image for the final Galinstan 3D microstructures after applying a high flow rate of 1000 µL min^{-1} to remove the excess Galinstan droplets remained in the channel. J) Top view of the 3D Galinstan microstructures using an optical microscope. K) SEM image of the 3D Galinstan microstructures.

Step two: The obtained Galinstan microdroplet suspension is applied to a DEP platform, as shown in Figure 1D,D′. The platform has eight pairs of planar chromium/gold (50/150 nm) microelectrode pads with a diameter of 80 μm patterned on a glass substrate (only three pairs of pads are shown in schematics). A circular chromium/gold island with a diameter of 80 μm is patterned between each pair of microelectrode pads, with a gap of 40 μm between the pads and the islands. The surface of the glass substrate, which is not patterned with microelectrode pads or islands is covered with a 500 nm SU8 layer using lithography processes to prevent the sticking of Galinstan microdroplets to gold microelectrodes (see Figure S2 in the Supporting Information for detailed design of the DEP platform). A polydimethylsiloxane (PDMS) microfluidic channel with a width and height of 600 and 80 μm, respectively, is integrated onto the DEP platform to facilitate the flow of suspension.

Figure 1E,E′ shows the immobilization of Galinstan microdroplets between the microelectrode pads 10 s after applying a sinusoidal signal with a magnitude and frequency of 15 V and 20 MHz, respectively. Galinstan microdroplets experience a very strong positive DEP force due to their high electrical conductivity (3.46×10^6 S m^{-1}).[30]

The DEP force exhibited on spherical Galinstan microdroplets can be calculated as[31]

$$\overline{F}_{\mathrm{DEP}} = 2\pi r^3 \varepsilon_{\mathrm{medium}} \mathrm{Re}[f_{\mathrm{CM}}] \nabla E^2 \quad (1)$$

where r is the radius of the microdroplets, $\varepsilon_{\mathrm{medium}}$ is the permittivity of the suspending medium, E is the applied electric field, and $\mathrm{Re}[f_{\mathrm{CM}}]$ is the real part of Clausius–Mossotti factor of the microdroplets, describing their polarization with respect to the surrounding medium.

In order to calculate the DEP force, we calculate the contours of electric field (E), and the gradient of electric field square (∇E^2), as detailed in Figure S3 (Supporting Information). According to our simulations, the magnitude of the DEP force exhibited on 2 μm Galinstan microdroplets reaches a maximum of 16.9 pN over the glass surface, and reduces to 5.56 pN at a levitation height of z = 10 μm (with respect to the glass surface), as shown in Figure S3 (Supporting Information). This force is strong enough to overcome the hydrodynamic drag force, pushing the microdroplets moving close to the glass surface toward the microelectrodes.

A relatively high flow rate of 50 μL min^{-1} is applied to enable the even distribution of Galinstan microdroplets along the eight consecutive microelectrode pads. A higher density of microdroplet clusters can be achieved by elongating the immobilization period, as shown in Figure 1F,F′. After the desired density of Galinstan microdroplet cluster is achieved, the magnitude of the applied signal and the flow rate are reduced to 5 V and 1 μL min^{-1}, respectively.

Step three: The inlet reservoir is then washed with SDS solution (2 mg mL^{-1}) to remove any remained Galinstan microdroplets. Then sodium hydroxide (NaOH) solution with a concentration of 0.1 mol L^{-1} is flushed through the microfluidic channel to remove the native oxide on the surface of Galinstan microdroplets, allowing them to merge and form larger droplets, as shown in Figure 1G,G′. This also allows the microdroplets to amalgamate the gold microelectrode pads.[12] By increasing the magnitude of the applied signal to 10 V, the electrochemical reaction between the NaOH solution and Galinstan droplets facilitates the amalgamation process. This enables the Galinstan droplets to quickly spread and wet the surface of the gold microelectrode pads, and form spherical cap with a small contact angle (<90°), as shown in Figure 1H,H′. Voltage magnitude larger than 11 V should be avoided, as this may electrochemically damage the microelectrodes by electrolyzing the NaOH solution. Finally, a high flow rate of 1000 μL min^{-1} is applied to remove the unmerged Galinstan droplets, and the Galinstan 3D microstructures are ready to use, as shown in Figure 1I,I′.

The entire process for forming Galinstan 3D microstructures is shown in Movie S1 (Supporting Information). This process can be repeated until the desired height of 3D microstructures is achieved. The top view images of the Galinstan 3D microstructures obtained using optical microscope and SEM are given in Figure 1J,K, respectively. It can be seen that all microelectrode pads are covered with Galinstan spherical caps with a relatively uniform height.

In order to characterize the height and uniformity of the obtained Galinstan 3D microstructures given in Figure 1, we use the 3D microstructures as the mould and pour PDMS onto them. The top view of a cured PDMS block with the patterned 3D microstructures imprinted is given in **Figure 2**A (see Figure S4 in the Supporting Information for details). This allows us to indirectly measure the height of the Galinstan spherical caps using a probe profiler. As an example, Figure 2B shows the depth profile along the red dashed line given in Figure 2A. The height of the Galinstan 3D microstructures obtained with 20 s immobilization period (Figure 1F′) is ranging from 25 to 40 μm, which can be changed to 17 ± 10, 29 ± 12, 50 ± 21, and 61 ± 24 μm by varying the immobilization period to 10, 20, 30, and 40 s, respectively, as shown in Figure 2C. Considering that the pad diameter is 80 μm, 3D microstructures with an aspect ratio (height/diameter) of up to ≈1 can be achieved by setting the immobilization period to 40 s, as shown in Figure 2D.

Furthermore, we investigate the capability of our method for making 3D microstructures with different diameters. In doing so, we reduce the diameter of the planar microelectrode pads from 80 to 60 and eventually 10 μm, and follow the procedure given in Figure 1, while maintaining the gap between the pads and the islands to 40 μm and setting the immobilization period to 20 s. Figure 2E shows the obtained height of Galinstan 3D microstructures with respect to different pad diameters ranging from 80 to 20 μm. Our results show that an aspect ratio of ≈0.3 can be achieved for all cases. However, when the pad diameter is reduced to 10 μm, we observe that some electrode pads are not covered by liquid metal after applying a high flow rate of 1000 μL min^{-1} to remove the unmerged Galinstan droplets (Step three). This means that the minimum diameter of the 3D microstructures obtained by our method is 20 μm.

3. Enabling 3D Microelectrodes for Trapping Suspended Particles

We further demonstrate the capability of 3D Galinstan microstructures to serve as 3D microelectrodes to trap suspended nanoparticles by means of DEP. The 3D microelectrodes have

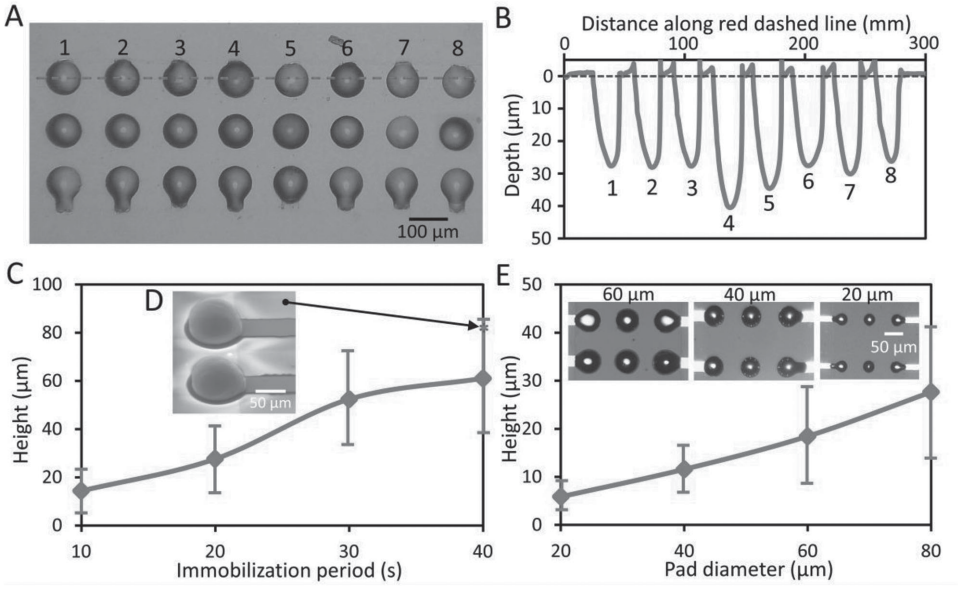

Figure 2. Characterization of the 3D Galinstan microstructures. A) Top view of a PDMS block cured by using the patterned 3D Galinstan microelectrodes as the mould. B) Depth profile of the PDMS block along the red dashed line. C) Microelectrode height versus immobilization period plot, obtained when DEP microelectrodes with a pad diameter of 80 µm are used, while the magnitude and frequency of the applied sinusoidal signal are set to 15 V and 20 MHz, respectively. D) SEM image for two 3D Galinstan microstructures with an aspect ratio of ≈1 by setting the immobilization period to 40 s. E) Microelectrode height versus electrode pad diameter, obtained with a 20 s immobilization period, while the magnitude and frequency of the applied sinusoidal signal are set to 15 V and 20 MHz, respectively. The insets show the top view of the 3D Galinstan microstructures with different pad diameters.

a pad diameter of 80 µm and a height of 30 µm (corresponding to 20 s immobilization period, as shown in Figure 2C). WO_3 nanoparticle (≈80 nm diameter) suspension with a concentration of 1 mg mL^{-1} is applied to the microfluidic channel at a flow rate of 20 µL min^{-1}. The 3D microelectrodes are energized by applying a sinusoidal signal with a magnitude and frequency of 15 V and 1 MHz, respectively, to trap nanoparticles. A similar process is followed to examine the trapping efficiency of planar (2D) microelectrodes and compare it with the case of 3D microelectrodes. The 2D microelectrodes have a pad diameter of 80 µm. **Figure 3**A,B shows the mass of WO_3 nanoparticles immobilized over the 2D and 3D microelectrodes, respectively, just 60 s after the activation of electric field.

To compare the trapping performance of 2D and 3D microelectrodes, we monitor the trapping process for a duration of 60 s, and calculate the surface area of glass covered by trapped WO_3 nanoparticles using image processing. The areas of microelectrode pads and islands (as shown with white dashed lines in Figure 3A,B) are excluded from the captured dark areas to ensure the enhanced trapping of 3D microelectrodes is due

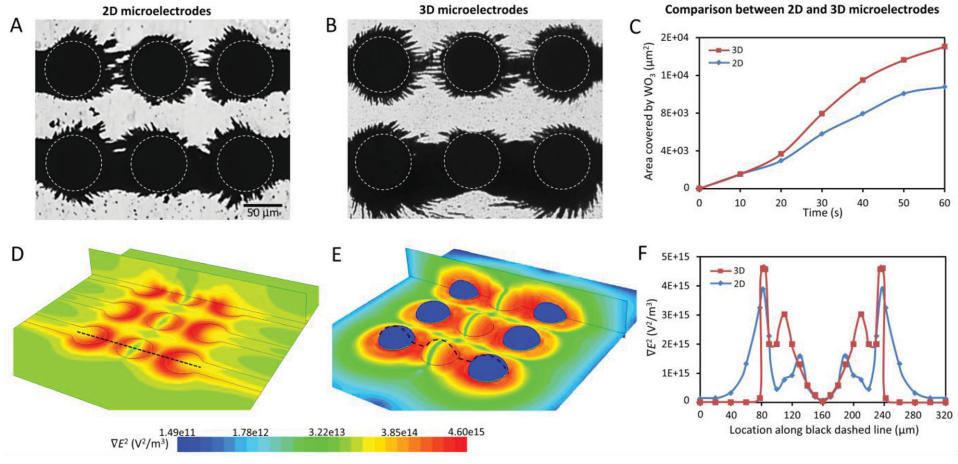

Figure 3. Comparison of planar and 3D DEP microelectrodes. Immobilization of WO_3 nanoparticles using A) planar and B) 3D microelectrodes, 60 s after the activation of electric field, with the flow rate set to 20 µL min^{-1}, and the magnitude and frequency of the applied signal set to 15 V and 1 MHz, respectively. C) Surface area of glass substrate covered by WO_3 nanoparticles versus time for planar and 3D microelectrodes. Contours of ∇E^2 for D) planar and E) 3D microelectrodes, obtained from numerical simulations. F) Variation of ∇E^2 along the black dashed lines.

to their enhanced electric field gradient, and not their larger surface area. The results clearly indicate the superior trapping efficiency of 3D microelectrodes (Figure 3C). For example, after 60 s, the area covered by the WO_3 nanoparticles over the glass substrate is ≈40% larger than that of planar microelectrodes.

A set of numerical calculations is carried out to comprehend the superior trapping efficiency of 3D microelectrodes. The DEP force experienced by a particle is proportional to the magnitude of ∇E^2, according to Equation (1). Figure 3D,E illustrates the contours of ∇E^2, produced by the 2D and 3D microelectrodes at the bottom surface of the microfluidic channel, and at the cross section of the microfluidic channel. The contours indicate the existence of strong ∇E^2 along the edges of pads and islands for both 2D and 3D microelectrodes. More importantly, the contours reveal the extension of strong field gradients between the pads and islands for the case of 3D microelectrodes. To further investigate this matter, we investigate the variations of ∇E^2 along a representative line which passes through the middle of 2D and 3D microelectrodes (shown as black dashed lines drawn in Figure 1D,E), as shown in Figure 3F. This graph indicates the existence of strong ∇E^2 along the edges of pads and the middle island (e.g., located at ≈80 and 120 μm) for both 2D and 3D microelectrodes. The average value of ∇E^2 between the two peaks (corresponding to the region between the edges of pads and the middle island) is calculated as 1.66×10^{15} V^2 m^{-3} for 2D microelectrodes and 2.78×10^{15} V^2 m^{-3} for 3D microelectrodes, indicating the superiority of 3D microelectrodes for generating strong field gradients over extended regions of the microfluidic channel. A similar trend is observed at other levitation heights of the microfluidic channel.

4. Enabling 3D Microstructures for Enhancing Heat Dissipation

We also demonstrate the capability of 3D Galinstan microstructures to enhance the convective heat transfer in a microfluidic channel. In doing so, we design a proof-of-concept experiment, which incorporates a microsized resistive heater integrated beneath a DEP based microfluidic platform to serve as a hot spot.

The DEP based microfluidic platform schematically shown in **Figure 4**A has the same specifications presented in Figure 1. The microsized resistive heater is fabricated by patterning a serpentine shaped resistor with an overall dimensions of 600 × 600 μm on a glass slide with a thickness of 1 mm (detailed design is given in Figure S5 in the Supporting Information), as shown in Figure 4B, and is energized by applying a DC voltage to generate a hot spot. Next, the DEP platform is attached onto the microsized heater such that the DEP microelectrodes are located on the top of the heater (detailed setup is given in Figure S6 in the Supporting Information). The temperature distribution across the bottom surface of the DEP platform is monitored by using an infrared (IR) camera, as shown in Figure 4C.

Figure 4D shows the schematic of heat dissipation through the microfluidic system. The heat is dissipated via the forced convection occurring due to the continuous stream of liquid through the microfluidic channel, and also via the free convection occurring across the free surfaces of glass and PDMS, as given below

$$Q_{\text{heater}} = \dot{m} C_{\text{p}} (T_{\text{out}} - T_{\text{in}}) + h A (\overline{T}_{\text{s}} - T_{\infty})|_{\text{glass}} + h A (\overline{T}_{\text{s}} - T_{\infty})|_{\text{PDMS}} \quad (2)$$

where $\dot{m}$ is the mass flow rate, C_{p} is the heat capacity, while T_{out} and T_{in} are the temperatures of the liquid at the outlet and inlet of the microfluidic channel, respectively, h is the free convection coefficient, which is assumed to be 10 W m^{-2} K^{-1}, A is the area of the surface in contact to ambient air, while $\overline{T}_{\text{s}}$ and T_{∞} are the average temperature of the surface and the ambient temperature, respectively. Considering the low thermal conductivity of PDMS, the last term on the right-hand side of Equation (2) can be ignored.

Galinstan has a thermal conductivity of 16.5 W m^{-1} K^{-1} which is much higher than those of glass and water. Therefore, we hypothesize that patterning an array of 3D Galinstan microstructures above the hot spot can effectively direct more heat into the stream of liquid flowing through the microfluidic channel, and enhances the convective heat transfer, as shown in Figure 4E.

In order to verify our hypothesis, we conduct experiments by applying flow rates of 20 and 60 μL min^{-1} to the microfluidic channel with or without 3D Galinstan microstructures. The heater is energized with a DC signal to provide a hot spot with a temperature of 40.5 °C on the top side of the heater, as monitored by the IR camera, as shown in Figure 4C (see Figure S5 in the Supporting Information). However, the temperature of the microsized heater recorded through the bottom side of the glass substrate is 37.1 °C due to the conductive heat dissipation though the glass.

We first conduct experiments by applying DI water at a flow rate of 20 μL min^{-1} into the channel. The temperature of the liquid at the inlet of the channel is measured as 23.4 °C. The obtained temperature contour is shown in Figure 4F. The direction of flow is from left to right. The measured temperature contours reveal the extension of orange (30–34 °C) and purple (28–30 °C) regions throughout the glass surface. The temperature of liquid reaches 24.1 °C at the outlet of the channel while the average temperature of the glass substrate is calculated as 23.9 °C. According to Equation (2), these values correspond to a heat loss of 2.79 mW along the microfluidic channel due to forced convection, and a heat loss of 1.40 mW across the free surface of the glass substrate due to free convection.

Following the procedures given in Figure 1, Galinstan 3D microstructures are formed on the gold pads and islands. Extensive numerical simulations are performed to comprehend the flow velocity profile in the presence of 3D Galinstan microstructures, as given in Figure S7 (Supporting Information). Our simulations reveal the formation of locally high velocity regions between the microstructures, and the repeated change of the flow velocity between the consequent microstructures, which can both influence the convective heat transfer through the microfluidic channel.

We carefully increase the current of the DC power supply to maintain the temperature of the hot spot at 40.5 °C while the flow rate of liquid is maintained at 20 μL min^{-1}. The captured temperature contours shown in Figure 4G indicate the better propagation of heat through the glass substrate, as evidenced by the progression of orange and purple regions toward the outlet of the microfluidic channel. The outlet temperature of the liquid reaches 25.5 °C leading to a heat loss of 4.32 mW

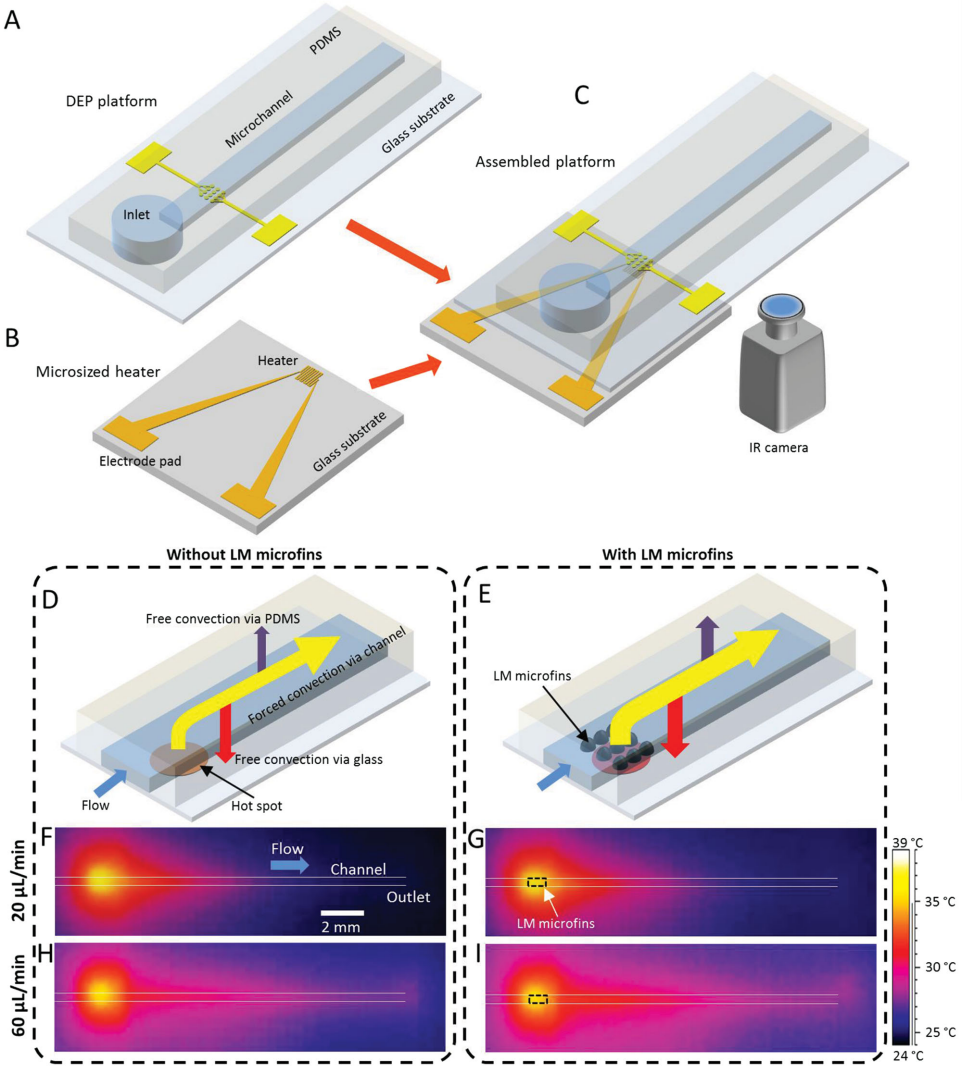

Figure 4. Applying the 3D Galinstan microstructures for heat dissipation from a hot spot. A) Schematics of the DEP platform. B) Schematic of the microsized heater. C) Assembled platform, in which the DEP system is placed on the top of the microsized heater, and an IR camera is utilized for monitoring temperature. Schematic for heat transfer when a microfluidic platform D) without LM microstructures or E) with LM microstructures in the channel are placed on the top of the hot spot, while the same temperature of the hot spot is maintained. Temperature contours obtained for the bottom of the microfluidic platform F,G) without and with LM microstructures at a flow rate of 20 µL min^{-1}, H,I) without and with LM microstructures at a flow rate of 60 µL min^{-1}.

through the main channel, and the average temperature of glass substrate is calculated as 25.9 °C leading to a heat loss of 2.51 mW through the glass substrate. The overall heat transfer is 6.83 mW, indicating an ≈63% increase compared to the case of without LM microstructures.

The oxide layer, which forms over the surface of Galinstan microstructures in the presence of DI water, has a thermal conductivity of 8.8 ± 3.4 W m^{-1} K^{-1},[32] which is lower than that of Galinstan, and therefore suppresses the heat transfer over the surface. However, the thickness of the oxide layer is in the range of 0.7–3 nm,[27–29] which minimizes its thermal effect. The temperature drop across the oxide layer can be estimated as $\Delta T = q'' \cdot t/k$, where q'' is the heat flux over Galinstan microstructures, and t and k are the thickness and thermal conductivity of the oxide layer, respectively, as detailed in Figure S8 (Supporting Information).

We also conduct experiments at a higher flow rate of 60 µL min^{-1}. Similarly, the current of the DC power supply is increased to maintain the temperature of the hot spot at 40.5 °C. Increasing the flow rate of the liquid enhances the forced convection through the channel, as evidenced by further extension of orange and purple contours throughout the glass surface (Figure 4H). This increases the outlet temperature and the average temperature of the glass substrate to 28.5 and 26.8 °C, respectively. Consequently, the heat dissipated through the channel and the free surface of the glass substrate increase to 21.33 and 3.40 mW, respectively.

Figure 4I shows the temperature contours in the presence of LM microstructures. We can clearly see that the presence of LM microstructures enhances the propagation of heat transfer rate, and increases the outlet and the average temperature of the

glass substrate to 29.4 and 28.0 °C, respectively. In this case, the heat dissipated through the channel and across the glass substrate increases to 25.09 and 4.58 mW, respectively, indicating an overall ≈20% enhancement compared to the case of without LM microstructures. The reduced enhancement of heat transfer at this high flow rate compared to the case when a low flow rate of 20 μL min^{-1} is applied can be attributed to the increased forced convection through the channel. Therefore, microstructures with a larger surface area are needed in order to further enhance the heat transfer rate for maintaining the similar enhancement of heat transfer, which can be achieved by either increasing the number of microstructures or increasing their dimensions.

To further explore the role of 3D Galinstan microstructures on enhancement of convective heat transfer, we conduct additional experiments by energizing the resistive heater with a constant DC signal. Experiments are conducted by applying DI water at a flow rate of 40 μL min^{-1} into the microfluidic channel with the results given in Figure S9 (Supporting Information). Under these conditions, the temperature of hot spot reaches a maximum of 37 °C in the absence of Galinstan microstructures (Figure S9A, Supporting Information), and reduces to 36.7 °C in the presence of Galinstan microstructures (Figure S9B, Supporting Information), indicating the improved propagation of heat through the microfluidic platform. To compare the temperature contours, we investigate the variations of temperature along five arbitrary lines that are parallel to the microfluidic channel, with the first line located along the center of the channel, and the gap between the lines set to 300 μm (Figure S9C, Supporting Information). According to this graph, the presence of Galinstan microstructures decreases the temperature of hot spot, whereas increases the temperature in the middle regions of the microfluidic system. This is in line with the results shown in Figure 4, and further confirms the enhanced convective heat transfer via the channel, which leads to better propagation of heat through the entire system, and avoids the accumulation of heat at the hot spot.

Additionally, we conduct several experiments to assess the capability of our technique to create Galinstan-based micromixers to agitate the surrounding liquid, as recently demonstrated by our group in ref. [12]. Our experiments indicate that the size of Galinstan microstructures has to be in the range of several hundred micrometers in order to achieve reasonable disturbance within the surrounding liquid, as shown in Figure S10 (Supporting Information). More investigation is required to improve the efficiency of the micromixer.

Despite the capability of our technique for creating controllable 3D Galinstan microstructures, the utilization of such microstructures in future microfluidic systems might be hampered by the variable thickness and wrinkling of the oxide layer, dissolving of gallium into the surrounding medium,[11] causing contamination and limiting their applications for biology related experiments, the high cost of liquid metals, and the low mechanical stability of microstructures.

5. Conclusion

In summary, we develop a novel method for creating 3D Galinstan microstructures using dielectrophoresis. We demonstrate the capability of our method for creating Galinstan 3D microstructures with different aspect ratios and sizes. We further use the microstructures as 3D DEP microelectrodes to immobilize WO_3 nanoparticles, and show their superior trapping efficiency compared to planar microelectrodes. The experimental results are interpreted by performing numerical simulations, which indicate that 3D microelectrodes are able to generate stronger DEP force compared to that of planar microelectrodes. Moreover, we develop a proof-of-concept experiment to show that our method can be used for creating Galinstan microfins to enhance the convective heat transfer within a microfluidic channel.

Our technique is parallel, allowing liquid metal to be deposited onto multiple locations simultaneously. It also has the potential for fine granularity—if the amount of Galinstan microdroplets in flow can be precisely controlled, then these can be added to the created liquid metal structures—allowing precise "dosing" of the amount of liquid metal added to each structure. We envisage that our proposed method for creating controllable 3D liquid metal microstructures has the potential to realize highly complex, yet practical applications in the areas of microfluidics, and microelectromechanical systems (MEMS), such as making 3D master moulds for soft-lithography processes,[25] forming flexible electrical interconnects and thermal interfaces,[3,13] heavy metal ion sensing,[8,9] as well as energy harvesting.[33]

6. Experimental Section

Experiment Setup: The planar microelectrodes and resistive heater were fabricated by depositing thin layers of chromium/gold (50/150 nm) on a thin glass slide (W × L × H = 24 mm × 60 mm × 100 μm) and patterned using standard photolithography techniques.[34] The PDMS microfluidic channel was fabricated using conventional soft lithography techniques,[34] and integrated onto the glass slides accommodating the microelectrodes. Microelectrodes were energized by a signal generator (Tabor, 2572A 100 MHz Dual-Channel) with one of the electrodes grounded. A syringe pump (Harvard, PHD 2000) was used to withdraw the liquid suspensions through the microfluidic channel at desired flow rates. The DEP platform was placed on an inverted microscope (Nikon Eclipse Ti) equipped with an electron-multiplying CCD camera (QuantEM 512SC) to monitor the experimental process.

Solution/Suspension Preparation: WO_3 nanoparticles suspension was prepared by dispensing 5 mg (China Rare Ltd.) of WO_3 nanoparticles into 5 mL of DI water and dispersing it using a high intensity ultrasonic processor (GEX500) for 30 min. NaOH solution was prepared by dissolving 100 mg solid NaOH into 25 mL of DI water.

Thermal Imaging: The temperature for the bottom of the platform was monitored using an infrared camera (FLIR Systems, ThermoVision A320, Sweden) interfaced with ThermaCAM Researcher software (ThermoVision).

Characterization: SEM images were taken using a FEI Nova NanoSEM. A probe profiler (Ambios XP200) was used to characterize the depth of the holes patterned on PDMS blocks.

Numerical Simulations: The numerical simulations were conducted using ANSYS Fluent 6.3 software package (Canonsburg, PA, USA).

Supporting Information

Supporting Information is available from the Wiley Online Library or from the author.

Acknowledgements

K.K. acknowledges the Australian Research Council for funding under Discovery Early Career Researcher Award (DECRA) scheme (Project No. DE120101402). The authors acknowledge the facilities, and the scientific and technical assistance, of the Australian Microscopy & Microanalysis Research Facility at the RMIT Microscopy & Microanalysis Facility, at RMIT University.

Received: March 31, 2015
Revised: May 9, 2015
Published online: June 9, 2015

[1] M. D. Dickey, R. C. Chiechi, R. J. Larsen, E. A. Weiss, D. A. Weitz, G. M. Whitesides, *Adv. Funct. Mater.* **2008**, *18*, 1097.
[2] T. Liu, P. Sen, C.-J. Kim, *J. Microelectromech. Syst.* **2012**, *21*, 443.
[3] E. Palleau, S. Reece, S. C. Desai, M. E. Smith, M. D. Dickey, *Adv. Mater.* **2013**, *25*, 1589.
[4] S.-Y. Tang, V. Sivan, K. Khoshmanesh, A. P. O'Mullane, X. Tang, B. Gol, N. Eshtiaghi, F. Lieder, P. Petersen, A. Mitchell, *Nanoscale* **2013**, *5*, 5949.
[5] V. Sivan, S.-Y. Tang, A. P. O'Mullane, P. Petersen, K. Kalantar-Zadeh, K. Khoshmanesh, A. Mitchell, *Appl. Phys. Lett.* **2014**, *105*, 121607.
[6] J. H. So, H. J. Koo, M. D. Dickey, O. D. Velev, *Adv. Funct. Mater.* **2012**, *22*, 625.
[7] S. Zhu, J. H. So, R. Mays, S. Desai, W. R. Barnes, B. Pourdeyhimi, M. D. Dickey, *Adv. Funct. Mater.* **2013**, *23*, 2308.
[8] W. Zhang, J. Z. Ou, S. Y. Tang, V. Sivan, D. D. Yao, K. Latham, K. Khoshmanesh, A. Mitchell, A. P. O'Mullane, K. Kalantar-zadeh, *Adv. Funct. Mater.* **2014**, *24*, 3799.
[9] V. Sivan, S. Y. Tang, A. P. O'Mullane, P. Petersen, N. Eshtiaghi, K. Kalantar-zadeh, A. Mitchell, *Adv. Funct. Mater.* **2013**, *23*, 144.
[10] W. Zhang, B. S. Naidu, J. Z. Ou, A. P. O'Mullane, A. F. Chrimes, B. J. Carey, Y. Wang, S.-Y. Tang, V. Sivan, A. Mitchell, S. K. Bhargava, K. Kalantar-zadeh, *ACS Appl. Mater. Interfaces* **2014**, *7*, 1943.
[11] S.-Y. Tang, K. Khoshmanesh, V. Sivan, P. Petersen, A. P. O'Mullane, D. Abbott, A. Mitchell, K. Kalantar-zadeh, *Proc. Natl. Acad. Sci. U.S.A.* **2014**, *111*, 3304.
[12] S.-Y. Tang, V. Sivan, P. Petersen, W. Zhang, P. D. Morrison, K. Kalantar-zadeh, A. Mitchell, K. Khoshmanesh, *Adv. Funct. Mater.* **2014**, *24*, 5851.
[13] J.-H. So, M. D. Dickey, *Lab Chip* **2011**, *11*, 905.
[14] S. H. Jeong, A. Hagman, K. Hjort, M. Jobs, J. Sundqvist, Z. Wu, *Lab Chip* **2012**, *12*, 4657.
[15] R. K. Kramer, C. Majidi, R. J. Wood, *Adv. Funct. Mater.* **2013**, *23*, 5292.
[16] Y. Zheng, Z. He, Y. Gao, J. Liu, *Sci. Rep.* **2013**, *3*, 1786.
[17] M. G. Mohammed, A. Xenakis, M. D. Dickey, *Metals* **2014**, *4*, 465.
[18] Y. Zheng, Q. Zhang, J. Liu, *AIP Adv.* **2013**, *3*, 112117.
[19] C. Ladd, J. H. So, J. Muth, M. D. Dickey, *Adv. Mater.* **2013**, *25*, 5081.
[20] Y. Liao, J. Song, E. Li, Y. Luo, Y. Shen, D. Chen, Y. Cheng, Z. Xu, K. Sugioka, K. Midorikawa, *Lab Chip* **2012**, *12*, 746.
[21] H. N. Chan, Y. Chen, Y. Shu, Y. Chen, Q. Tian, H. Wu, *Microfluid. Nanofluid.* **2015**, DOI: 10.1007/s10404-014-1542-4.
[22] M. Z. Bazant, Y. Ben, *Lab Chip* **2006**, *6*, 1455.
[23] M. Nasabi, K. Khoshmanesh, F. J. Tovar-Lopez, K. Kalantar-zadeh, A. Mitchell, *Electrophoresis* **2013**, *34*, 3150.
[24] I.-F. Cheng, V. E. Froude, Y. Zhu, H.-C. Chang, H.-C. Chang, *Lab Chip* **2009**, *9*, 3193.
[25] J. Fang, W. Wang, S. Zhao, *Encyclopedia of Microfluidics and Nanofluidics*, Springer US, New York, USA **2008**, pp 645–656.
[26] J. N. Hohman, M. Kim, G. A. Wadsworth, H. R. Bednar, J. Jiang, M. A. LeThai, P. S. Weiss, *Nano Lett.* **2011**, *11*, 5104.
[27] M. Regan, H. Tostmann, P. S. Pershan, O. Magnussen, E. DiMasi, B. Ocko, M. Deutsch, *Phys. Rev. B* **1997**, *55*, 10786.
[28] F. Scharmann, G. Cherkashinin, V. Breternitz, C. Knedlik, G. Hartung, T. Weber, J. Schaefer, *Surf. Interface Anal.* **2004**, *36*, 981.
[29] A. Plech, U. Klemradt, H. Metzger, J. Peisl, *J. Phys.: Condens. Matter* **1998**, *10*, 971.
[30] C. Karcher, V. Kocourek, D. Schulze, *Int. Sci. Colloq. Modell. Electromagn. Process.* **2003**, 105.
[31] H. Morgan, N. G. Green, *AC Electrokinetics: Colloids and Nanoparticles*, Research Studies Press, Philadelphia, PA, USA **2003**.
[32] C. J. Szwejkowski, N. C. Creange, K. Sun, A. Giri, B. F. Donovan, C. Constantin, P. E. Hopkins, *J. Appl. Phys.* **2015**, *117*, 084308.
[33] T. Krupenkin, J. A. Taylor, *Nat. Commun.* **2011**, *2*, 448.
[34] K. Kalantar-zadeh, B. Fry, *Nanotechnology-Enabled Sensors*, Springer US, New York, USA **2007**.